Research Article | Vol. 27, No. 3 | 4 Feb 2019 | OPTICS EXPRESS 2235
Optics EXPRESS

Endogenous SHG and 2PEF coherence imaging of substructures in neurons in 3D

CARLOS MACIAS-ROMERO, CLAIRE TEULON, MARIE DIDIER, AND SYLVIE ROKE*

Laboratory for fundamental BioPhotonics (LBP), Institute of Bioengineering (IBI), and Institute of Materials Science (IMX), School of Engineering (STI), and Lausanne Centre for Ultrafast Science (LACUS), École Polytechnique Fédérale de Lausanne (EPFL), CH-1015, Lausanne, Switzerland
**sylvie.roke@epfl.ch*

Abstract: Neuronal morphology, long-distance transport and signalling critically depend on the organization of microtubules in the cytoskeleton. Second harmonic generation (SHG) imaging has been recognized as a potentially powerful tool for *in situ* label-free neuroimaging with specific sensitivity to microtubules. We study here the structural organization of microtubules in living neurons using a wide-field multiphoton microscope that performs 3D imaging using a structured illumination. This microscope allows label-free high throughput imaging of living mammalian neurons. We show that we can image structural correlations by taking advantage of the structured illumination and the coherence of the emitted light. The result allows us to study the microtubule organization throughout the development of the neuron and to differentiate between the regions of the cytoskeleton in the matured neuron.

1. Introduction

The formation of living neuronal networks is largely determined by the dynamics of the cytoskeleton of the neurons [1]. The cytoskeleton is composed of microtubules, actin microfilaments and neurofilaments, which provide the cell with motility, structure, and an intracellular trafficking network. Microtubules are non-centrosymmetric biopolymers that extend into the processes of the neuron, i.e. the axon and dendrites, to create the trafficking network. Their polarity determines the direction in which certain cytoplasmic constituents are transported [2,3]. Each part of the cytoskeleton has different microtubule organizations [1,4]: Axons have well-aligned microtubules (all pointing in one direction), dendrites and the cell body cytoskeleton have more disordered microtubules, pointing in both directions with various degrees of orientational distributions [5], and the centrosome is composed of two orthogonal microtubule bundles surrounded by microtubules and proteins randomly oriented [6,7]. Understanding the role of microtubules organization and its dynamics is thus particularly important to assess developmental stages of neurons and to understand the mechanism of functional diversity, trafficking, regulation of the cytoskeleton and the mechanisms behind various neurodegenerative diseases [3,8].

Different methods exist to observe the organization of microtubules [9], such as the Hook method [10] or single molecule imaging [11]. Most of those methods are fluorescent-based, invasive and even destructive. The development of label-free imaging would allow an observation of intact neurons, as well as live cell imaging, and directly unravel the complex mechanisms ruling neuronal activity and growth. Some developments towards this goal have allowed for label-free observations of organelle transportation [12,13], cytoskeleton [14] or membrane potentials [15,16]. It has also been observed that some proteins involved in the metabolism of cells can display endogenous two-photon excited fluorescence (2PEF) [17]. Endogenous 2PEF arises from fluorophores such as NAD(P)H or flavoproteins present throughout the whole neuron but mostly concentrated in the soma [17]. Second harmonic generation (SHG) imaging [18] has been recognized as a non-invasive tool to determine the

#338351 https://doi.org/10.1364/OE.27.002235
Journal © 2019 Received 1 Aug 2018; revised 10 Sep 2018; accepted 10 Sep 2018; published 24 Jan 2019

Optics EXPRESS

overall polarity of microtubules bundles [5,19] in tissues, the axon, and the thickest dendrites of mature cultured neurons.

Here we expand on these developments by using a 3D wide-field multiphoton microscope. With this system, label-free 3D SHG imaging of an aqueous/solid interface with a demonstrated improvement of signal to noise ratio of ~5000 times compared to scanning confocal microscopy was achieved [20]. In this work, we explore the 3D imaging capabilities for neuroscience by imaging mammalian neurons in culture with 2PEF and SHG. We demonstrate the possibility of depth-sectioning, whereby the cytoskeleton and the soma can be observed within 1 second exposure. We then show that it is possible to take advantage of the different interference patterns observed with SHG. These patterns depend on the degree of coherence of the signal emitted by the sample. In particular, we exploit the effect of the coherence of the illumination and the degree of mutual polarization of the emitted light on the propagation of these patterns. We are interested here in the degree of mutual polarization because it varies with the structural correlations between microtubules in the different parts of the neuron, and therefore yields structural information about the cytoskeleton structure.

2. Two-beam illumination microscope: HiLo imaging for depth-sectioning

2.1 Optical setup

We recently developed a wide-field multiphoton microscope with two beams illumination [20]. The scheme of the setup is shown Fig. 1. The light source is an amplified Yb:KGW laser system (Pharos SP-1.5, Light Conversion) delivering 190 fs laser pulses centred around 1036 nm (± 6 nm) with a repetition rate of 200 kHz. To achieve wide-field 3D SHG imaging, we use a diffraction grating generated with a phase-only spatial light modulator (SLM, Holoeye, Pluto) to split the illuminating beam into beams at different angles (diffraction orders), as shown in Fig. 1(a). A filter is placed in the Fourier plane (Fig. 1(b)) of the SLM to retain only the + 1 and −1 diffraction orders. These two diffraction orders give rise to two beams that are incident on the sample plane at a certain angle (imaged with the aid of a relay system), yielding a cosine interference pattern at the sample plane (Fig. 1(c)). The spatial frequency σ of the diffraction grating on the SLM determines the angle of incidence of the beams on the sample and the spatial frequency k_g of the interference pattern illuminating the sample. The field of view, 150 µm (at full width at half maximum, FWHM), is determined by the spot size on the SLM and the overall magnification of the relay system. The objective lenses used for focusing of the excitation beams and collection of the SHG light are both water immersion with the following specifications: focusing – 60x, NA 1.0, 2 mm working distance, no coverslip correction (Olympus, LUMPLFLN 60XW); collection – 60x, NA 1.1, 1.5 mm working distance, variable coverslip correction (Olympus, LUMFLN 60XW). We used an angle $\delta = 11°$ for both of the two illumination beams (leading to a spatial frequency $k_g = 0.37$ μm^{-1} at focus), illumination beams in (YZ) plane, and a fluence of 3.5 mJ/cm^2. The sample is mounted on an XYZ translation stage (AsiImaging, PZ 2000). The imaging camera is a back-illuminated electron-multiplied and intensified CCD camera with 512 x 512 pixels (Princeton Instruments, PI-MAX4, 512EM-HBf P46 GENIII). The polarization of incident beams can be controlled. The image acquisition and all stages are controlled with a custom-made LabView interface.

The illumination configuration allows us to implement a HiLo procedure [21] to obtain depth sectioning. HiLo has been implemented successfully as a background rejection and 3D imaging technique for different configurations [22–25], and is more time efficient than structured illumination microscopy (SIM) [22,26,27].

Optics EXPRESS

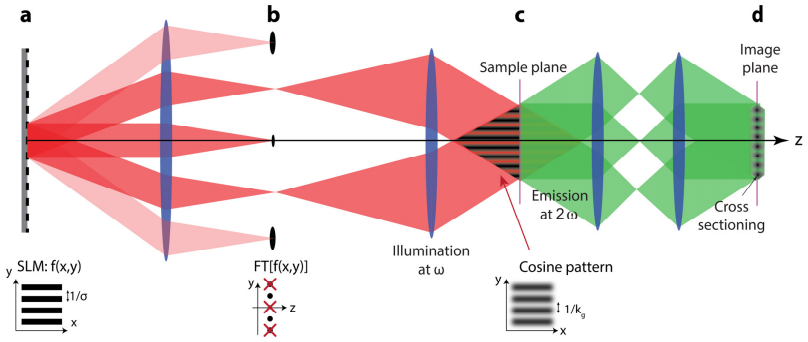

Fig. 1. Two beam illumination and the corresponding interference pattern. (a) The pattern displayed on the SLM is a grating of spatial frequency σ diffracting the incident beam. (b) The diffracted beams are filtered in the Fourier plane: only beams corresponding to ± 1 diffraction orders are kept. (c) Those two beams arrive with an incident angle δ on the sample, creating a cosine interference pattern with frequency k_g in the sample plane. (d) The sample plane is imaged on an IEM-CCD camera.

2.2 HiLo algorithm

In previously published HiLo algorithms [22,27] applied to fluorescence imaging, two images are taken to obtain depth sectioning: one that is uniformly illuminated I_u, and one that is illuminated with a pattern containing a single spatial frequency I_n. This method relies on the visibility of the interference pattern of the emitted light decaying quickly with defocus [21]. The uniformly illuminated image I_u contains both in-focus and out-of-focus content. To reject the out-of-focus content, it suffices to apply a high-pass filter to the image, thereby selecting only high spatial frequency components, which arise inherently from the in-focus content. The patterned image I_n is spatially modulated by the illumination pattern and, more importantly, contains the low- and high-frequency information from the object, but only from the volumetric cross-section in which the interference pattern is visible. A demodulation algorithm is needed to extract the low-frequency information and then combine it with the high-frequency information to obtain the final cross-sectioned image.

Several demodulation algorithms can be used to extract the low-frequency information that is modulated by the pattern. Here we use the algorithm presented in refs [22,27–29]. In our case however, instead of using a randomized wavefront or changing the illumination conditions [21,22,28], we obtain the uniformly illuminated image by using two patterned images shifted in phase:

$$\begin{aligned} I_1 &= I_{in}\left[1+M\cdot\cos\left(k_g x\right)\right]+I_{out} \\ I_2 &= I_{in}\left[1+M\cdot\cos\left(k_g x+\pi\right)\right]+I_{out}, \end{aligned} \tag{1}$$

where I_{in} corresponds to signal from the image plane (in-focus content), I_{out} corresponds to signal from other planes (out-of-focus content), and M is a modulation factor. The uniformly illuminated image I_u is obtained by averaging those two images (as described in Appendix A, Fig. A1): $I_u = (I_1 + I_2)/2 = I_{in} + I_{out}$. The algorithm to obtain depth-sectioning is detailed in Appendix A and illustrated using a 2PEF imaging stack recorded from a cortical neuron in primary culture. Visualization 1 and Visualization 2 are giving the corresponding 2PEF and SHG 3D image stacks processed with this algorithm.

3. Axial resolution and coherence of light

As mentioned previously [20], the HiLo method relies on the visibility of the interference pattern decaying quickly with defocus [21]. This visibility depends on the degree of coherence [30,31] of the emitted light, as illustrated in Fig. 2. This figure shows the different

Optics EXPRESS

interference patterns along the optical axis (along Z) for three different degrees of coherence. Figure 2(a) shows how the imaged interference pattern changes along depth when the degree of coherence changes. Figure 2(b) shows what resolution can be expected from the HiLo procedure in those cases. If the emitted light is fully coherent (top image), the axial intensity distribution in the image space consists of repeating interference patterns along the optical axis (shifted by $\pi/2$). In this case no depth-sectioning can be obtained. If the emission is partially coherent, the fringe visibility decreases significantly before and after the image plane at Z = 0 (middle image). This effect can yield depth sectioning but with the possibly important presence of side lobes. If the emission is fully incoherent, the side lobes are absent, yielding a clean depth sectioning (bottom image). This is the case for fluorescence imaging [17,30].

The relationship between the visibility of the interference patterns in the image space and the degree of coherence of the light can be explained by describing the light emitted by the object using planes waves [30]. If the emission is fully coherent (top panel), the field at the camera is composed only of the three plane waves depicted in Fig. 1(d). In this case, we see an interference pattern throughout the whole depth range. If the emission is partially coherent, multiple uncorrelated sets of these three plane waves are emitted at different angles. While the three plane waves within each set always have a fixed angular relation and always add in phase, the multiple sets have different angles between them and add in intensity. The lower the degree of coherence, the larger the angular range is between the multiple sets of plane waves. A broader angular range decreases the visibility of the fringes along the optical axis, and thus improves the axial resolution.

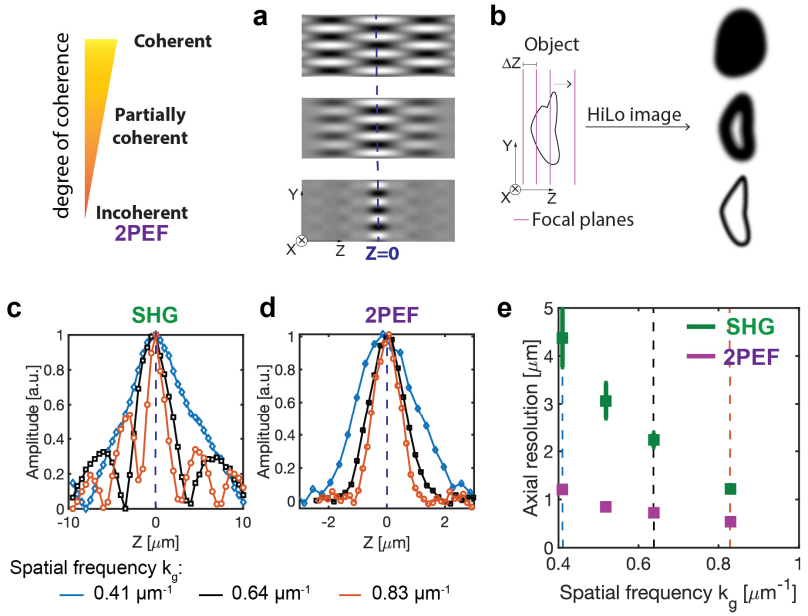

Fig. 2. Axial resolution of the microscope and coherence. (a) Interference pattern in the image space depending on the degree of coherence of the emitted light. Here the pattern is shown for fully coherent light, partially coherent light and incoherent light. (b) The HiLo algorithm relies on the visibility of the interference pattern: all depths displaying an interference pattern will show in the HiLo image, limiting its axial resolution. (c) SHG signal from one hBN monolayer deposited on a 20 nm thick SiNx film on a Si wafer as a function of imaging depth, for three different spatial frequencies k_g. (d) 2PEF signal from a 200nm Trypan Blue slab as a function of imaging depth, for three different spatial frequencies k_g. (e) Measured axial resolutions for SHG from hBN (in green) and 2PEF from Trypan blue (in magenta), for different spatial frequencies k_g.

Optics EXPRESS

To explore the conditions for which HiLo depth sectioning is possible using partially or fully coherent light, we imaged the SHG signal from a hexagonal boron nitrate (hBN) monolayer, and the 2PEF signal from a ~200 nm thick slab of Trypan blue dye dissolved in water at different depths. Figure 2(c) shows the axial distributions from the hBN measurement for different spatial frequencies k_g of the patterned illumination at the sample. Even though the SHG signal from hBN is expected to be highly coherent [32] the observed interference pattern has a finite depth, which is much shorter than the depth expected from the laser pulse (60 μm) [33]. Such finite depth is due to the chirp in the illumination laser, which lowers the coherence of the illumination [20,21], yielding a degree of coherence 0.8. To depict the fully incoherent case, Fig. 2(d) shows the axial distributions from imaging the slab of Trypan blue dye.

Figure 2(e) shows the measured axial resolutions for SHG from hBN (in green) and 2PEF from Trypan blue (in magenta) as a function of the spatial frequency of the interference pattern k_g. The resolution is defined here as the half width at half maximum (HWHM) of the distributions. It can be seen from Fig. 2(e) that the axial resolution obtained with SHG and 2PEF is different for the same spatial frequency k_g: the axial resolution obtained with 2PEF, an incoherent signal, is higher. Nonetheless, the SHG signal can still be exploited to produce cross-sections and derive structural information in a sample. Note that the axial resolution depends on the spatial frequency k_g, i.e. on the angle between the two incident beams. The higher the spatial frequency is, the better is the axial resolution.

In what follows we explore how the extent of the interference in the axial direction reveals information useful for neuroimaging. We show what kind of information we can obtain from endogenous 2PEF and SHG from neurons, and the possibility of 3D imaging. We are interested in particular in the information that the SHG signal can give us about the structural correlations between microtubules, the polar building blocks of the cytoskeleton.

4. Sample preparation and imaging

4.1 Cell culture preparation

Primary cultures of cortical neurons were prepared from E17 OF1 mice embryos of either sex. Briefly, embryos were decapitated, and brains removed and placed in PBS-glucose. Cortices were removed under a dissecting microscope and collected in a small Petri dish in PBS-glucose. A single-cell suspension was obtained by gentle trituration with a fire-polished Pasteur pipette in Neurobasal medium supplemented with B27 and GlutaMAX (Invitrogen, phenyl red free). Cells were plated at an average density of 15,000 cells/cm^2 in supplemented Neurobasal medium on polyornithine-coated glass coverslips (20 mm diameter). After 3–4 h, coverslips were transferred to dishes containing glial cell monolayers in supplemented Neurobasal medium. Neurons were maintained at 37°C in a humidified atmosphere of 95% air – 5% CO2, and the neuron observed was 32 days *in vitro*. All experimental protocols were approved by Service de la consommation et des affaires vétérinaires, canton de Vaud, Suisse (authorizations 882.8 and 882.9). All methods were carried out in accordance with relevant guidelines and regulations.

4.2 Cell imaging

The cells were imaged at room temperature in an open flow chamber under physiological conditions [34]. The neuron was confirmed to be alive after the measurements by monitoring in wide-field configuration a physiological reaction (i.e. expansion-contraction) to the buffer solution enriched with potassium (50mM). The association of the SHG signals to the microtubules was corroborated by exposing the neurons to the depolymerizing drug nocodazole [5,19,35]. Microtubules treated with nocodazole are destabilized and depolymerize. For a neuron treated with nocodazole, the measured SHG signal decreases significantly and recover after a wash out.

Optics EXPRESS

We imaged living primary cultured neurons (Fig. 3). Figure 3(a) shows the phase contrast (PC) image of unstained cultured neurons (28DIV: 28 days *in vitro*). The image displays a cell body from which several neurites (arrows) and one axonal-like neurite (arrow head) have emerged. The corresponding 2PEF and SHG signals are shown in Fig. 3(b). The composite image is shown in Fig. 3(c). The 2PEF intensity is represented in blue, and the SH intensity either in red (with a polarization along the X direction, projected on the sample plane) or in blue (with a projection along the Y direction).

Then, we recorded label-free 3D SHG and 2PEF images at 41 different depths, 0.5 µm apart. SHG images were made with an acquisition time of 10 s per image and a 515 ± 10 nm bandpass filter (FL514.5-10, Thorlabs), and were obtained with 0XX and 0YY polarization configurations, i.e. excitation with a linear polarization along X (resp. Y) for both beams, and detection without an analyser to preserve the information given by the degree of mutual polarisation. Coherence determination was performed over the average of the two polarization-resolved image stacks. Endogenous 2PEF image stacks were made with an acquisition time of 100 ms per image, using a 550 nm long pass filter (FEL550, Thorlabs). For both techniques, the excitation light was filtered out with a 910 nm short pass filter (ET910SP, Chroma). The measurement time of all modalities (performed sequentially) was ~15 minutes.

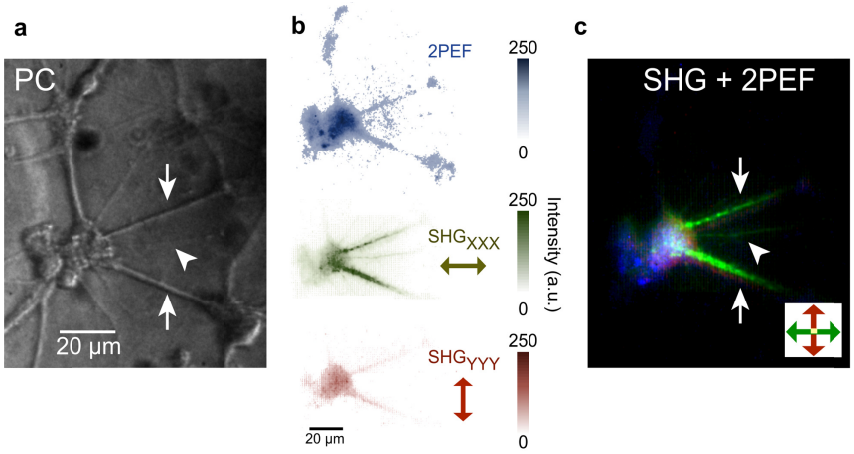

Fig. 3. Label-free TPEF and SHG imaging of living neurons. (a) Phase contrast (PC) image of mouse brain neurons. The two arrows show dendrites and the arrow head the axon, (b) Top panel: endogenous 2PEF signal averaged over 100 frames, with 639 ms/frame. Middle and bottom panels: SH images, in green obtained with an excitation and detection polarization direction along the X axis (XXX), and in red obtained with an excitation and detection polarization direction along the Y axis (YYY). Both images are averaged over 100 frames, acquired with 639 ms/frame and a power on sample around 125 mW. (c) Composite image with label-free SHG XXX and YYY in green and red respectively, and endogenous 2PEF in blue.

5. Degree of coherence as measure of structural correlations

Figure 4(a) presents an illustration of the microtubule (represented by arrows) orientation in the different parts of the cytoskeleton. The expected fringes visibility [30,31] depends on the degree of coherence of the emitted light, which can change with both the degree of coherence of the excitation light and the degree of mutual polarization [30] of the emitted light, describing spatial correlations of the emitters. We show additionally in Fig. 4(a) the expected degree of mutual polarization for each microtubule organization. If we illuminate any of these structures, we can expect to observe different fringe visibilities along the axial direction. That is because the degree of mutual polarization of the emitted light is affected by the structural correlations in the sample. The degree of mutual polarization is maximum if we illuminate a

Optics EXPRESS

sample with aligned dipoles, like aligned microtubules in axons, with coherent light. If we use the same light source to illuminate a more disordered structure, like microtubules in dendrites, the degree of mutual polarization is lower and the fringe visibility along Z decays faster resulting in an improved resolution. The degree of mutual polarization is zero for randomly distributed emitters: the fringe visibility along the Z direction decays very quickly, resulting in the best resolution possible.

Thus, the fringe visibility of the observed 2PEF/SHG emission depends on both the organization of the light emitters of the object and on the degree of coherence of the illumination. Figure 4 shows structured illumination images taken at different depths in a cultured cortical neuron with SHG (Fig. 4(b-d), corresponding to Visualization 3) and 2PEF (Fig. 4(e-g), corresponding to Visualization 4) as well as the corresponding phase contrast image of this neuron (Fig. 4(h)). Note that the SHG and 2PEF images are the unprocessed structured images. It can be seen that interference patterns are only present for Z = 0 for the case of 2PEF (Fig. 4(f)), while the interference pattern appears on all three images for the SHG signal. The reason is that 2PEF is incoherent [30], so that the fringes present in the illuminating light are negated by the random distribution and temporal incoherence of the fluorescent emitters. On the other hand, second harmonic generation (SHG) can possess higher degrees of coherence. A non-centrosymmetric structure with a high structural correlation generates a highly coherent SHG signal (high degree of mutual polarization), which will interfere over a large axial range. On the contrary, a structure with almost no structural correlation will generate a highly incoherent SHG signal (low degree of mutual polarization), which will lower the axial range of the fringe visibility to one plane only.

Since all the non-resonant emission is instantaneous, we are obtaining information about the spatial and temporal correlations of the nonlinear emitters in the neuron, in particular the structural correlations of the microtubules in the neurons.

To observe the structural correlations between microtubules, we plot in Fig. 4(i) a map of the structural correlations obtained from the SHG image stacks. This is done using the average of the two image stacks (41 different depths, 0.5 μm apart) taken with orthogonal polarization configurations to probe all microtubules orientations. Each image was HiLo processed and binned in the (XY) plane. The HiLo-processed stacks would then contain the necessary depth information (pixel-wise) to obtain the extent of the decay in the fringe visibility and thus proceed to calculate the structural correlations.

The extent of the fringe visibility across the whole field of view was obtained by fitting the axial intensity distribution of each pixel with a Gaussian function. Each pixel could then be associated with the full-width at half maximum (FWHM) of its Gaussian fit, which is proportional to fringe visibility along the optical axis of the given pixel. Only fits with good enough quality (r-square > 0.7) were kept. A large FWHM corresponds to a high degree of structural correlations (yellow) and a small FWHM corresponds to a low degree of structural correlations (blue). The γ scale on Fig. 4(i) is constructed as follows: A fully unperturbed interference (maximum obtainable FWHM, limited by the coherence of the illumination) results in $\gamma = 1$, while a minimal FWHM (corresponding to the FWHM measured for 2PEF incoherent signal) is linked to $\gamma \sim 0$.

Optics EXPRESS

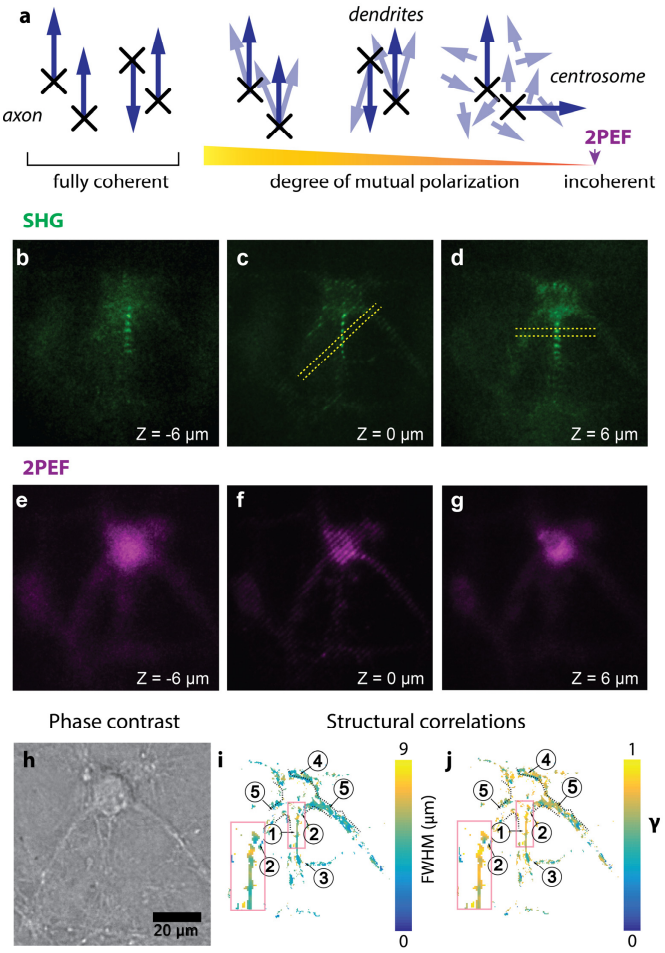

Fig. 4. The degree of mutual polarization gives information about structural organization. (a) Scheme of microtubules organizations in different parts of the cytoskeleton and their corresponding expected degree of mutual polarization for the SHG signal. Images of a cortical neuron at different depths with structured illumination: (b-d) SHG and (e-g) endogenous 2PEF. Visualization 3 and Visualization 4 are the corresponding 3D image stacks. (h) Corresponding white light phase contrast image. (i) Map of the FWHM of the obtained interference pattern. (j) Map of the degree of structural correlations γ, proportional to the axial resolution (FWHM) of the SHG signal emitted by the microtubules in the neuron.

The observation of the phase contrast image (Fig. 4(h)) does not allow us to differentiate parts of the cytoskeleton morphology of the neuron. Examining more closely the SHG structured illuminated images (Visualization 3), for the three different imaging planes shown Fig. 4(b-d), it can be seen that an interference pattern, located along feature #1, remains in focus even after 6 µm of defocus (Figs. 4(b) and 4(d)), while no other feature in the image displays such behaviour. This means that only feature #1 structure displays orientational correlations, generating an interference pattern with a wide axial range. It is therefore the only structure containing well-aligned microtubules and can therefore be assigned to be the axon. Feature #2 shows the lowest degree of coherence, and is therefore likely composed of microtubules with orthogonal orientations, as it is expected in the centrosome [7]. Finally, features #5 (and #4) show a medium degree of coherence, consistent #5 and #4 being dendrites and the cytoskeleton of the soma composed of slightly disordered microtubules.

The measurement of the degree of coherence of the SHG signal allows therefore probing of the microtubules organization in neurons label-free, since it depends on both the degree of coherence of the excitation light and on the degree of mutual polarization in the sample. It is possible to classify structural variations in different parts of the cytoskeleton and to observe neuronal morphology, which is not possible with phase contrast imaging.

6. Conclusions

To conclude, SHG and 2PEF coherence 3D imaging were performed on living mammalian neurons using a high throughput wide-field multiphoton microscope. We demonstrated the possibility of depth-sectioning with structured illumination adapted from HiLo imaging [21], and showed the axial resolution that could be achieved for 2PEF or SHG imaging. This depth-sectioning can be used to perform 3D imaging. We then implemented a coherence mapping to achieve label-free and non-invasive imaging of structural orientational correlations and showed we can apply it to image the morphology of the microtubules network in a mammalian cortical neuron. This label-free and non-invasive technique allows therefore to image neuronal morphology. It can be combined with SHG polarization-resolved measurements to obtain most information about microtubules organization in the cytoskeleton.

Moreover, good signal to noise ratio can be obtained within ~10 s / 100 ms acquisition times (SHG/2PEF), paving the way for dynamic imaging. Given the improvement of throughput and the availability of nonlinear light scattering instrumentation and theory needed to quantify individual microtubules, label-free dynamic *in vitro* imaging of microtubules is a possibility for the near future.

This 3D label-free imaging technique would therefore be interesting for neuroimaging given that it allows to probe the neurons with different modes of contrast that highlight different aspects of their morphology. We showed that the observed SHG signal probes the organization of the cytoskeleton. As SHG has an intrinsic sensitivity to electrostatic potentials [20] it might be also possible to perform label-free imaging of electrical activity. Finally, the observation of the endogenous 2PEF entails the possibility of observing mitochondrial respiration of living cells in real time, label free, opening the possibility of mapping cell metabolism and synaptic activity that way.

Appendix A: detailed HiLo procedure

We describe here in more detail the HiLo algorithm used to obtain a depth-sectioned image from the two patterned images I_1 and I_2 (displayed Fig. 5(a)).

The procedure to obtain the low-frequency depth-sectioned image is described Fig. 5(b). We use the image difference $\frac{I_1 - I_2}{2} = M \cdot I_{in} \cdot cos\left(k_g x\right)$, in order to remove part of the noise of the image already. Most of the out-of-focus content I_{out} is indeed removed from this image, and the image information about in-focus content in the image (I_{in}) is shifted around $\pm k_g$ grating frequencies. We first apply a high-pass filter of very low cut-off frequency to this image to remove the remaining noise at very low frequencies, and obtain a denoised image I_d. Then, calculating an absolute value of this image, $|I_d|$, allows to bring back the image information around zero frequency in Fourier space (we now have three peaks at $-k_g$, k_g and 0). It is straightforward to apply a low pass filtering with the cut-off frequency k_c to this image, in order to finally obtain I_{Lo}, the image containing the low-frequencies in-focus components of the neuron. The cut-off frequency k_c is typically set at $\sim \frac{k_g}{2}$ [28].

The procedure to obtain the high frequency depth-sectioned image, I_{Hi}, is described Fig. 5(c). We apply a high-pass filter to the uniform image. The high-pass filter used is the

Optics EXPRESS

complementary to the low-pass filter used for the I_{Lo} image, to make sure all frequencies are recovered in the final image. The result of this filtering is the I_{Hi} image, which contains only the high-frequency components. The HiLo image (I_{HiLo}), displayed Fig. 5(d), is the final depth-sectioned image resulting from the weighted addition of the low- and high- frequency images: $I_{HiLo}=I_{Hi}+\mu I_{Lo}$. The weighting is done empirically to aid the transition between low and high frequencies [22,27]. The weighting value μ depends on the spatial cut-off frequencies of all the filters. The raw data was processed with a HiLo algorithm written in Matlab [20]. The parameters used here are: μ=3, k_c=0.18 μm^{-1} and cut-off frequency 3.10^{-2} μm^{-1} to remove noise. The cosine pattern at the sample has a spatial frequency of k_g= 0.37 μm^{-1}.

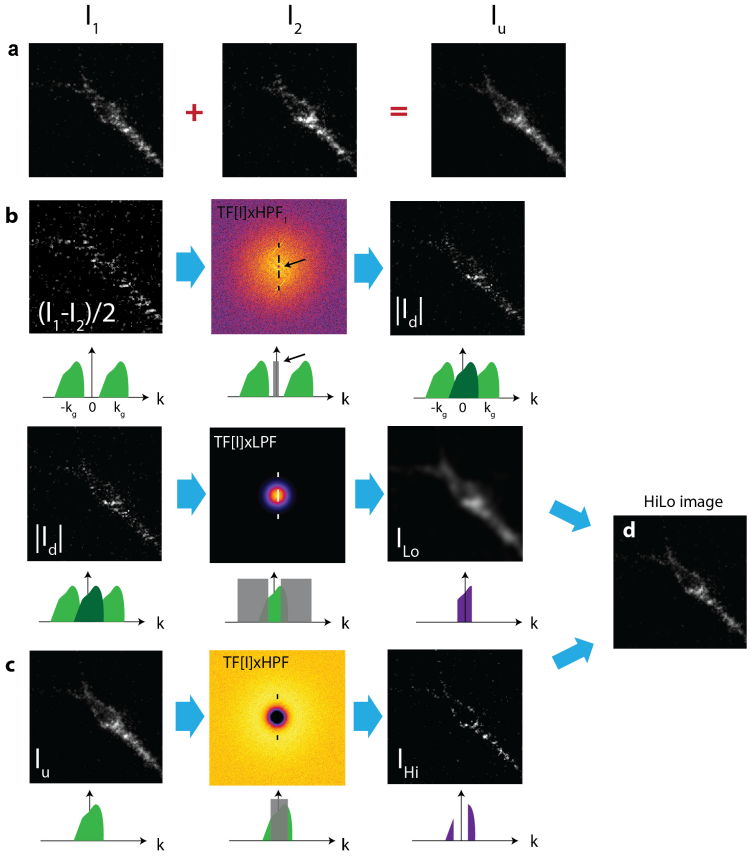

Fig. 5. Principle of the HiLo algorithm used here. A scheme of the information content in the Fourier space (along the dashed line) is given under each image. Images in Fourier space are in colors, while images are black and white. (a) Two structured illumination images with shifted interference patterns are recorded, I_1 and I_2. The sum of those two images gives a "uniform illumination" image I_u. (b) Lo image: (top) a structured illumination image is firstly denoised with a low cut-off frequency high-pass filter: this allows to remove noise at low frequency; (bottom) we take the absolute value of the denoised image to bring back image information around 0 frequency, then we apply a low-pass filter on this image to obtain the Lo image. (c) Hi image: a high-pass filter (complementary of the low-pass filter) is applied on the uniform illumination image to obtain the Hi image. (d) Hi and Lo images are summed to obtain the final HiLo image.

Appendix B: Volumetric rendering

Figures 6 and 7 show snapshots of the 3D SHG (Fig. 6) and 2PEF (Fig. 7) movies."

Optics EXPRESS

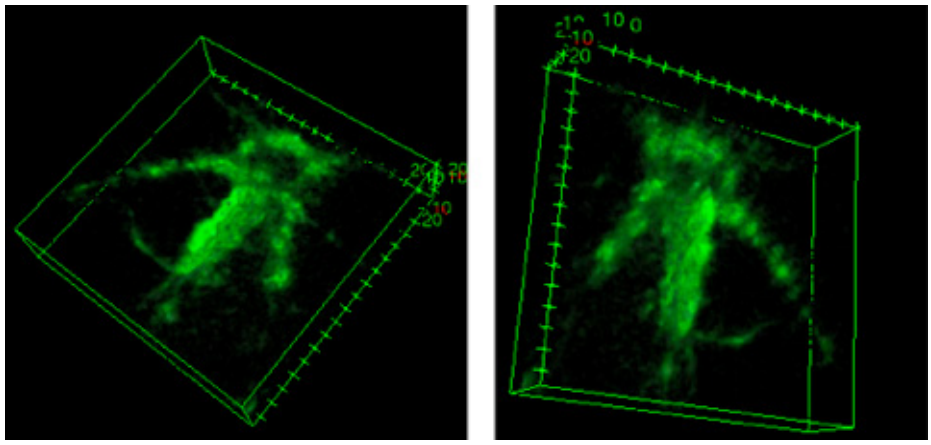

Fig. 6. Snapshot of a video showing the reconstructed 3D SHG response. The axon is much wider than its actual size, due to the high degree of coherence.

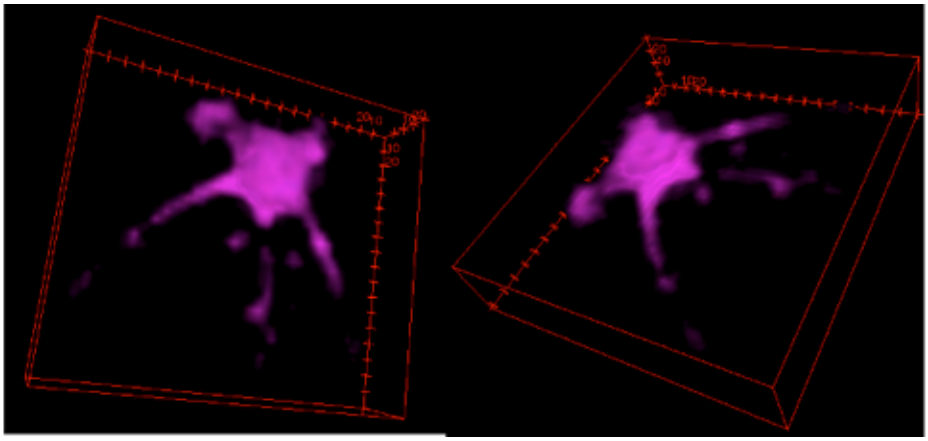

Fig. 7. Snapshot of a video showing the reconstructed 3D 2PEF response.

Funding

Julia Jacobi Foundation, the Swiss National Foundation (200021-146884); European Commission, Research Executive Agency Marie Curie Actions 'FINON' (ITN-2013-607842).

Acknowledgments

The authors acknowledge Pascal Jourdain and Pierre Magistretti for providing the neurons and helping with the neuroscientific material, and Aleksandra Radenovic for discussions and providing the hBN sample. Supplementary material is available in the online version of the paper. Four visualizations are provided. Correspondence and requests for materials should be addressed to S.R.

References

1. E. R. Kandel, J. H. Schwartz, and T. M. Jessell, Principles of neural science (McGraw-hill, 2000), Vol. 4.
2. P. W. Baas, "Microtubules and neuronal polarity: lessons from mitosis," Neuron **22**(1), 23–31 (1999).
3. L. C. Kapitein and C. C. Hoogenraad, "Which way to go? Cytoskeletal organization and polarized transport in neurons," Mol. Cell. Neurosci. **46**(1), 9–20 (2011).
4. C. Conde and A. Cáceres, "Microtubule assembly, organization and dynamics in axons and dendrites," Nat. Rev. Neurosci. **10**(5), 319–332 (2009).

Optics EXPRESS

5. A. C. Kwan, D. A. Dombeck, and W. W. Webb, "Polarized microtubule arrays in apical dendrites and axons," Proc. Natl. Acad. Sci. U.S.A. **105**(32), 11370–11375 (2008).
6. M. Kuijpers and C. C. Hoogenraad, "Centrosomes, microtubules and neuronal development," Mol. Cell. Neurosci. **48**(4), 349–358 (2011).
7. M. Stiess, N. Maghelli, L. C. Kapitein, S. Gomis-Rüth, M. Wilsch-Bräuninger, C. C. Hoogenraad, I. M. Tolić-Nørrelykke, and F. Bradke, "Axon extension occurs independently of centrosomal microtubule nucleation," Science **327**(5966), 704–707 (2010).
8. L. C. Kapitein and C. C. Hoogenraad, "Building the neuronal microtubule cytoskeleton," Neuron **87**(3), 492–506 (2015).
9. S. F. B. van Beuningen and C. C. Hoogenraad, "Neuronal polarity: remodeling microtubule organization," Curr. Opin. Neurobiol. **39**, 1–7 (2016).
10. P. W. Baas, M. M. Black, and G. A. Banker, "Changes in microtubule polarity orientation during the development of hippocampal neurons in culture," J. Cell Biol. **109**(6), 3085–3094 (1989).
11. R. P. Tas, A. Chazeau, B. M. C. Cloin, M. L. A. Lambers, C. C. Hoogenraad, and L. C. Kapitein, "Differentiation between oppositely oriented microtubules controls polarized neuronal transport," Neuron **96**(6), 1264–1271 (2017).
12. M. E. Kandel, D. Fernandes, A. M. Taylor, H. Shakir, C. Best-Popescu, and G. Popescu, "Three-dimensional intracellular transport in neuron bodies and neurites investigated by label-free dispersion-relation phase spectroscopy," Cytometry A **91**(5), 519–526 (2017).
13. Y. Yang, H. Yu, X. Shan, W. Wang, X. Liu, S. Wang, and N. Tao, "Label□free tracking of single organelle transportation in cells with nanometer precision using a plasmonic imaging technique," Small **11**(24), 2878–2884 (2015).
14. P. Bon, S. Lécart, E. Fort, and S. Lévêque-Fort, "Fast label-free cytoskeletal network imaging in living mammalian cells," Biophys. J. **106**(8), 1588–1595 (2014).
15. X. W. Liu, Y. Yang, W. Wang, S. Wang, M. Gao, J. Wu, and N. Tao, "Plasmonic□based electrochemical impedance imaging of electrical activities in single cells," Angew. Chem. Int. Ed. Engl. **56**(30), 8855–8859 (2017).
16. H. J. Lee, D. Zhang, Y. Jiang, X. Wu, P.-Y. Shih, C.-S. Liao, B. Bungart, X.-M. Xu, R. Drenan, E. Bartlett, and J.-X. Cheng, "Label-free vibrational spectroscopic imaging of neuronal membrane potential," J. Phys. Chem. Lett. **8**(9), 1932–1936 (2017).
17. W. R. Zipfel, R. M. Williams, R. Christie, A. Y. Nikitin, B. T. Hyman, and W. W. Webb, "Live tissue intrinsic emission microscopy using multiphoton-excited native fluorescence and second harmonic generation," Proc. Natl. Acad. Sci. U.S.A. **100**(12), 7075–7080 (2003).
18. F. S. Pavone and P. J. Campagnola, Second Harmonic Generation Imaging (CRC Press, 2013), p. 476.
19. D. A. Dombeck, K. A. Kasischke, H. D. Vishwasrao, M. Ingelsson, B. T. Hyman, and W. W. Webb, "Uniform polarity microtubule assemblies imaged in native brain tissue by second-harmonic generation microscopy," Proc. Natl. Acad. Sci. U.S.A. **100**(12), 7081–7086 (2003).
20. C. Macias-Romero, I. Nahalka, H. I. Okur, and S. Roke, "Optical imaging of surface chemistry and dynamics in confinement," Science **357**(6353), 784–788 (2017).
21. M. A. A. Neil, R. Juškaitis, and T. Wilson, "Real time 3D fluorescence microscopy by two beam interference illumination," Opt. Commun. **153**(1-3), 1–4 (1998).
22. J. Mertz and J. Kim, "Scanning light-sheet microscopy in the whole mouse brain with HiLo background rejection," J. Biomed. Opt. **15**(1), 016027 (2010).
23. E. Y. Yew, H. Choi, D. Kim, and P. T. So, "Wide-field two-photon microscopy with temporal focusing and HiLo background rejection," in SPIE BiOS, (International Society for Optics and Photonics, 2011), 79031O–79031O–79036.
24. E. Muro, P. Vermeulen, A. Ioannou, P. Skourides, B. Dubertret, A. Fragola, and V. Loriette, "Single-shot optical sectioning using two-color probes in HiLo fluorescence microscopy," Biophys. J. **100**(11), 2810–2819 (2011).
25. M. A. Lauterbach, E. Ronzitti, J. R. Sternberg, C. Wyart, and V. Emiliani, "Fast calcium imaging with optical sectioning via HiLo microscopy," PLoS One **10**(12), e0143681 (2015).
26. M. G. L. Gustafsson, "Nonlinear structured-illumination microscopy: wide-field fluorescence imaging with theoretically unlimited resolution," Proc. Natl. Acad. Sci. U.S.A. **102**(37), 13081–13086 (2005).
27. S. Santos, K. K. Chu, D. Lim, N. Bozinovic, T. N. Ford, C. Hourtoule, A. C. Bartoo, S. K. Singh, and J. Mertz, "Optically sectioned fluorescence endomicroscopy with hybrid-illumination imaging through a flexible fiber bundle," J. Biomed. Opt. **14**(3), 030502 (2009).
28. D. Lim, K. K. Chu, and J. Mertz, "Wide-field fluorescence sectioning with hybrid speckle and uniform-illumination microscopy," Opt. Lett. **33**(16), 1819–1821 (2008).
29. J. Michaelson, H. Choi, P. So, and H. Huang, "Depth-resolved cellular microrheology using HiLo microscopy," Biomed. Opt. Express **3**(6), 1241–1255 (2012).
30. E. Wolf, Introduction to the Theory of Coherence and Polarization of Light (Cambridge University, 2007).
31. E. Hecht, Optics, IVth ed. (Addison-Wesley, 2001).
32. A. Nagashima, N. Tejima, Y. Gamou, T. Kawai, and C. Oshima, "Electronic structure of monolayer hexagonal boron nitride physisorbed on metal surfaces," Phys. Rev. Lett. **75**(21), 3918–3921 (1995).
33. J. C. Diels, J. J. Fontaine, I. C. McMichael, and F. Simoni, "Control and measurement of ultrashort pulse shapes (in amplitude and phase) with femtosecond accuracy," Appl. Opt. **24**(9), 1270 (1985).

Optics EXPRESS

34. P. Jourdain, N. Pavillon, C. Moratal, D. Boss, B. Rappaz, C. Depeursinge, P. Marquet, and P. J. Magistretti, "Determination of transmembrane water fluxes in neurons elicited by glutamate ionotropic receptors and by the cotransporters KCC2 and NKCC1: a digital holographic microscopy study," J. Neurosci. **31**(33), 11846–11854 (2011).
35. W. H. Stoothoff, B. J. Bacskai, and B. T. Hyman, "Monitoring tau-tubulin interactions utilizing second harmonic generation in living neurons," J. Biomed. Opt. **13**(6), 064039 (2008).